JAST, Vol. 14, No. 1, pp.

JAST Journal of Aerospace Science and Technology

Scientific-Research Article

Analysis of Composite Lattice Cylindrical Shells Under Transient Dynamic Loading

Ali Davar[1*], Mahdi Mehrbani[2], MohammadReza Zamani[3], Mohsen Heydari Bani[4], Jafar Eskandari Jam[5]

1, 3 & 5 – University Complex of Materials and Manufacturing Technology, Malek Ashtar University of Technology

2 & 4- Department of Mechanical Engineering, Malek Ashtar University of Technology

* ZIP Code :15875-1774 , Tehran, Iran

Email: *Davar78@gmail.com

The composite lattice cylindrical shells are analyzed in this research while they are subjected to transient dynamic loading. The equilibrium equations for the composite cylindrical shell are expressed in terms of classical shell theory. Additionally, due to the discontinuous distribution of stiffness and shell mass between reinforcing ribs and their proximity to one another (empty or filled with filler material), this issue has been expressed using an appropriate distribution function. On the basis of Lowe's first approximation theory, the strain-displacement and curvature-displacement relationships are considered. The Galerkin method is used to calculate the natural frequencies and shapes of structural modes for the boundary conditions, as well as the transient dynamic response of the composite cylindrical lattice shell to lateral impulsive loading applied extensively and uniformly on a specific rectangular surface. The convolution and a method for summing the effects of the modes are also obtained, and the obtained results are validated using references and ABAQUS finite element software. The effects of various parameters on free and forced vibrations are investigated, including geometric ratios, material properties, cross-sectional dimensions and distances, and lattice configuration. Finally, the effect of strengthening the cylindrical shell with lattice structures is investigated.

Keywords: *Analytical modeling, lattice, Rib, reinforced, internetworking distance, composite cylindrical shell*

Introduction

Composite structures are widely used in a variety of industries, including aerospace, marine, missile, and pressure vessel construction, due to their high Strength-to-weight ratio, resistance to moisture and corrosion, and other unique properties. Nevertheless, designers have considered composite shells as a frequently used structure for many years. Suzuki, Shikanai, and Chino [1] investigated the vibrations of composite circular cylindrical tanks in 1990 using power series and minimum Lagrangian

1 Assistant Professor, Corresponding Author
2 Holder of Master of Science
3 Assistant Professor
4 PhD Student
5 Professor

Received Date: 1 Jan 2021
Accepted Date: 12 July 2021

techniques. The frequency increases proportionately to the ratio of the inner-to-outer radius of a circular plate. The frequency of the outer circular plate increases as the length-to-outer radius ratio of the cylinder increases, and also the frequency decreases as the length-to-outer radius ratio of the cylinder increases. Lam and Loy [2] investigated the effect of boundary conditions on a thin-walled rotating cylindrical shell in their paper. Lowe's theory and the Galerkin method are applied in this study. Validation of the analysis is accomplished by comparing the results to those previously published by other researchers. The cylindrical shell under investigation is a three-layer shell with a [0/90/0] composition. The frequencies decrease initially and then increase as the number of peripheral waves increases. In 2001, Zhang [3] used the wave propagation method to analyze the vibrations of composite cylindrical shells under various Crass-ply boundary conditions. Saunders' theory is applied. He compared his findings to those of Lam and Loy, who obtained favorable results. In 2003, Lee et al. conducted an analytical and experimental analysis of the free vibration of a layered composite cylindrical shell. This theory makes use of the energy principle derived from classical plate (or shell) theory and Lowe's thin-shell (or plate) theory. To validate the original formulation, numerical results are compared to experimental results and a finite element analysis. It is worth noting that this research investigated the effects of the length-to-radius ratio, the radius-to-shell thickness ratio, and the angle of fiber placement on the natural frequencies of composite layered cylindrical shells using a parametric study [4].
In 2007, Ciavalek conducted a numerical study of the free vibrations of cylindrical and conical shells using the first hypothesis of Lowe's thin-shell theory and its solution via the discrete singular loop method. The effects of peripheral wave number and layer count on dynamic properties are discussed in this study. According to the application and results, this numerical method is appropriate, simple, and accurate [5]. Qatu and Asadi conducted a comprehensive study of shallow shell vibrations in 2012, examining 21 different boundary conditions. This study was conducted using thin-shell theory, and precise results for natural frequencies were obtained. The Ritz method is used to determine the natural frequencies of the shell under various boundary conditions, which results in the presentation of the natural frequencies of the shell under various curvatures [6].
Finally, in 2013, Ghavanloo and Fazelzadeh investigated shallow orthotropic shells with two curvatures and their free vibrations. In this study, the Novozhilov shallow shell theory is used, with the primary assumption being that the shell has a simply support condition. The cylindrical shells and hyperbolic parabolic spheres were presented in this study, and the results were compared numerically [7].
Finally, it's worth noting that both impregnation and finite element modeling methods for lattice structures have a number of constraints and, in addition to numerous errors, present researchers with optimization challenges. Additionally, a dearth of research on forced vibrations in all lattice structure geometries and the behavior of cylindrical panels subjected to impulsive loading has been noted.
As a result of the discontinuous distribution of the stiffness and mass of the shell between the reinforcing ribs and the distance between them (empty or filled with filler), this issue has been expressed in this study using an appropriate distribution function. In the case of integrated and lattice cylindrical shells, the results were validated against those of other researchers and also against those of numerical solutions obtained using ABAQUS software.

Methodology

Analytical modeling of reinforced composite structures

On the basis of prior research and the benefits of reinforced composite structures, it is entirely appropriate to consider reinforced structures as plates and shells with component distribution on the surface. In other words, the empty spaces formed by these structures can be treated as elastic components with a zero modulus. Indeed, both empty spaces and those filled with fillers can be regarded as integrated components analytically [8]. Reinforced shells are regarded in this research as sandwich structures composed of a lattice core (reinforcement), lower and upper (reinforced) surfaces, as illustrated in Fig. 1. The deformation of the sandwich shell is too low to satisfy the assumptions of Kirchhoff's classic theory. The next section extracts the equations and relations regulating cylindrical shells.

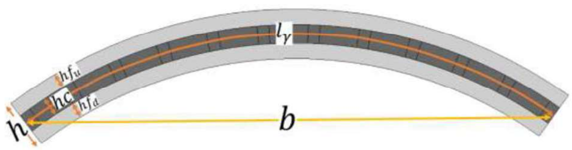

Fig. 1. Facing view Sandwich shell configuration consisting of core (amplifier) and external and internal procedures.

Strain-displacement and stress-strain relations

The mechanical displacement field for cylindrical shells in a cylindrical coordinate system can be represented as follows according to the selected shear deformation theory:

$$\varepsilon_\theta = \varepsilon_\theta^0 + rk_\theta \, , \varepsilon_x = \varepsilon_\theta^0 + rk_x \, , \gamma_{\theta x} = \gamma_{\theta x}^0 + r\tau \qquad (1)$$

Where the strain and curvature variations in the middle layer is as follows:

$$\varepsilon_{xx}^0 = \frac{\partial u}{\partial x} \qquad (2)$$

$$\varepsilon_{\theta\theta}^0 = \frac{1}{R}\frac{\partial v}{\partial \theta} + \frac{w}{R} \qquad (3)$$

$$\varepsilon_{x\theta}^0 = \frac{\partial v}{\partial x} + \frac{1}{R}\frac{\partial u}{\partial \theta} \qquad (4)$$

$$k_{xx} = \frac{\partial \beta_x}{\partial x} \qquad (5)$$

$$k_{\theta\theta} = \frac{1}{R}\frac{\partial \beta_\theta}{\partial \theta} \qquad (6)$$

$$k_{x\theta} = \frac{\partial \beta_\theta}{\partial x} + \frac{1}{R}\frac{\partial \beta_x}{\partial \theta} \qquad (7)$$

In which β_θ and β_x are as follows:

$$\beta_x = -\frac{\partial w}{\partial x} \qquad (8)$$

$$\beta_\theta = \frac{v}{R} - \frac{1}{R}\frac{w}{\partial \theta} \qquad (9)$$

The general stress-strain relation for k^{th} layer of composite multi-layer with fixed Stiffness matrix $\overline{Q}_{ij}$ as follows:

$$\begin{bmatrix} \sigma_\theta \\ \sigma_x \\ \sigma_{\theta x} \end{bmatrix}_k = \begin{bmatrix} \overline{Q}_{11} & \overline{Q}_{12} & \overline{Q}_{16} \\ \overline{Q}_{12} & \overline{Q}_{22} & \overline{Q}_{26} \\ \overline{Q}_{16} & \overline{Q}_{26} & \overline{Q}_{66} \end{bmatrix}_k \begin{bmatrix} \varepsilon_\theta \\ \varepsilon_x \\ \gamma_{\theta x} \end{bmatrix}_k \qquad (10)$$

The preceding relation is presented for the general case in which the principal coordinates axes do not coincide with the material principal axes. Stiffness matrix of the material $\overline{Q}_{ij}(\theta, x)$ in the cylindrical coordinate system and in the direction of the coordinate axes x and θ are varying for the reinforced sandwich shells. In this case, the fixed stiffness matrix $\overline{Q}_{ij}$ is written in terms of x and θ as $\overline{Q}_{ij}(\theta, x)$ for k^{th} layer. As illustrated in Fig. 2, the aforementioned relation is reformulated as follows for the lattice shell, which exhibits discontinuity in material properties in the direction of ribs, knots, and voids (or fillers).

$$\begin{bmatrix} \sigma_\theta \\ \sigma_x \\ \sigma_{\theta x} \end{bmatrix}_k = \begin{bmatrix} \overline{Q}_{11}(\theta, x) & \overline{Q}_{12}(\theta, x) & \overline{Q}_{16}(\theta, x) \\ \overline{Q}_{12}(\theta, x) & \overline{Q}_{22}(\theta, x) & \overline{Q}_{26}(\theta, x) \\ \overline{Q}_{16}(\theta, x) & \overline{Q}_{26}(\theta, x) & \overline{Q}_{66}(\theta, x) \end{bmatrix}_k \begin{bmatrix} \varepsilon_\theta \\ \varepsilon_x \\ \gamma_{\theta x} \end{bmatrix}_k \qquad (11)$$

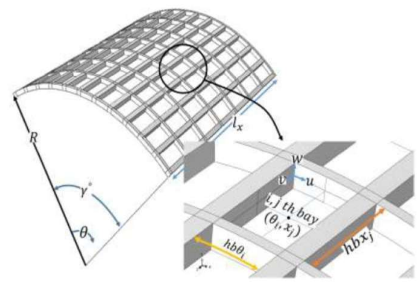

Fig. 2. Schematic and configuration of the orthogonal lattice shell.

Two-zone modeling (rib and empty space) and four-zone modeling (zero-degree rib, ninety-degree rib, knot, and empty space) were presented for the analysis of lattice shells. The stiffness matrices of the ribs and knots are the same and distinct from those of the vacant spaces in two-zone modeling (or filler materials). While the material is parallel to the zero- and ninety-degree ribs in four-zone modeling for characteristics and stiffness matrix, it is not parallel to the empty spaces (or filler materials). Additionally, the entire stiffness matrix of zero rib and ninety-degree rib is applied at the knot in this modeling such that the knot portions are more rigid than the ribs.

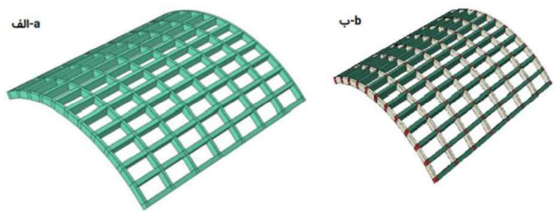

Fig. 3. a) Modeling of two areas (green: ribs - white: empty or filling areas) b) Modeling of four zones (green: 90-degree rib - milk: zero-degree rib - red: knot - white: empty areas or fillers).

As a result, the distribution function for the functional attributes of the two models was shown as follows:

$$\overline{Q}_{ij}(\theta, x, z) = \overline{Q}_{ijk}(\theta, x) = \overline{Q}^{1}_{ijk}[1 - HP^{0}(x)HP^{90}(\theta)] + \overline{Q}^{2}_{ijk}HP^{0}(x)HP^{90}(\theta) \quad (12)$$

The subscript k refers to k^{th} layer of the composite and the superscripts 1 and 2 refer to the property matrices of ribs and empty areas (or fillers), respectively.

Four areas (twisted string):

$$Q_{ij}(\theta, x, z) = Q_{ijk}(\theta, x) = Q^{0}_{ijk}[1 - HP^{0}(x)] + Q^{90}_{ijk}[1 - HP^{90}(\theta)] + Q^{2}_{ijk}HP^{0}(x)HP^{90}(\theta) \quad (13)$$

Where Q^{0}_{ijk}, Q^{90}_{ijk}, and Q^{2}_{ijk} refer to property matrix in the same direction as zero-degree rib, ninety-degree rib, and empty areas (or fillers).

The density distribution function is same for both models and is defined as follows.

$$\rho_{ijk}(\theta, x) = \rho^{1}_{ijk}[1 - HP^{0}(x)HP^{90}(\theta)] + \rho^{2}_{ijk}HP^{0}(x)HP^{90}(\theta) \quad (14)$$

The subscript k refers to k^{th} layer of the composite and the superscripts 1 and 2 refer to the property matrices of ribs and empty areas (or fillers), respectively.

The distribution function HP in x and θ direction is defined as follows:

$$HP^{0}(x) = \begin{cases} 1, \text{Outer zone of the zero} - \text{degree rib} \\ 0, \text{Zones on the zero} - \text{degree rib} \end{cases}$$

$$HP^{90}(x) = \begin{cases} 1, \text{Outer zone of the ninety} - \text{degree rib} \\ 0, \text{Zones on the ninety} - \text{degree rib} \end{cases}$$

The distribution function for the orthograde lattice shells is expressed using the Heaviside unit step function in HP.

$HP^{90}(\theta)$ and $HP^{0}(x)$ for the modelling in Fig. 3 are defined as follows:

$$HP^{0}(x) = 1\sum_{j=1}^{n_x} H\left(x - x_j - \frac{hbxj}{2}\right)$$

$$HP^{90}(\theta) = \sum_{i=1}^{m_\theta} H\left(\theta - \theta_i + \frac{hb\theta i}{2}\right) - H\left(\theta - \theta_i - \frac{hb\theta i}{2}\right) \quad (15)$$

n_x is the number of hollows along the axis x, and m_θ is the number of hollows in the peripheral direction of the shell. The total number of the hollows is equal to $n_x \times m_\theta$. Additional parameters are depicted in Fig. 2. Forces and moments are calculated using the following equations based on the aforementioned relationships:

$$\begin{bmatrix} N_\theta \\ N_x \\ N_{\theta x} \end{bmatrix} = \int_{-h/2}^{h/2} \begin{bmatrix} \sigma_\theta \\ \sigma_x \\ \sigma_{\theta x} \end{bmatrix} dr \quad (16)$$

$$\begin{bmatrix} M_\theta \\ M_x \\ M_{\theta x} \end{bmatrix} = \int_{-h/2}^{h/2} \begin{bmatrix} \sigma_\theta \\ \sigma_x \\ \sigma_{\theta x} \end{bmatrix} rdr \quad (17)$$

The following equation was obtained by incorporating the stress-strain relationships into the latter equation and integrating them over the thickness of the sandwich shell:

$$\begin{bmatrix} N_\theta \\ N_x \\ N_{\theta x} \\ - \\ M_\theta \\ M_x \\ M_{\theta x} \end{bmatrix} = \begin{bmatrix} A_{11}(\theta,x) & A_{12}(\theta,x) & A_{16}(\theta,x) & B_{11}(\theta,x) & B_{12}(\theta,x) & B_{16}(\theta,x) \\ A_{12}(\theta,x) & A_{22}(\theta,x) & A_{26}(\theta,x) & B_{12}(\theta,x) & B_{22}(\theta,x) & B_{26}(\theta,x) \\ A_{16}(\theta,x) & A_{26}(\theta,x) & A_{66}(\theta,x) & B_{16}(\theta,x) & B_{26}(\theta,x) & B_{66}(\theta,x) \\ - & - & - & - & - & - \\ B_{11}(\theta,x) & B_{12}(\theta,x) & B_{16}(\theta,x) & D_{11}(\theta,x) & D_{12}(\theta,x) & D_{16}(\theta,x) \\ B_{12}(\theta,x) & B_{22}(\theta,x) & B_{26}(\theta,x) & D_{12}(\theta,x) & D_{22}(\theta,x) & D_{26}(\theta,x) \\ B_{16}(\theta,x) & B_{26}(\theta,x) & B_{66}(\theta,x) & D_{16}(\theta,x) & D_{26}(\theta,x) & D_{66}(\theta,x) \end{bmatrix} \begin{bmatrix} \varepsilon^{0}_{\theta\theta} \\ \varepsilon^{0}_{xx} \\ \varepsilon^{0}_{\theta x} \\ - \\ k_{\theta\theta} \\ k_{xx} \\ k_{\theta x} \end{bmatrix} \quad (18)$$

The $A(\theta, x)$, $B(\theta, x)$, and $D(\theta, x)$ matrices, which are functions of x and θ, are referred to as axial stiffness, flexural stiffness (also called flexural rigidity), and coupling stiffness, respectively, and are equal to

$$\left(A(\theta, x), B(\theta, x), D(\theta, x)\right) = \sum_{k=1}^{n_l} \int_{r_{k-1}}^{r_k} \overline{Q}_{ijk}(\theta, x)(1, r, r^2)dr \quad (19)$$

n_l is the number of different layers on the sandwich shell thickness, and r_k and r_{k-1} are the distance between the outer and the inner k^{th} surfaces of the middle layer, respectively.

Equations of motion

The primary method for obtaining the governing equations on the sandwich panel is to calculate changes by minimizing the total energy stored in the body and the work done by external forces entering the body. The primary relationship between this method and the Hamilton equation is as follows:

$$\delta\int(U+V-T)dt=0 \tag{20}$$

In which U Denotes the structure's stored potential energy, V is the total energy from the work of external forces on the structure, T is kinetic energy which is equal to zero, and δ is the First-order shift operator. As a result of the variation equation and the corresponding equations, the extraction motion equations for the lattice sandwich shell are as follows [10]:

$$\frac{\partial N_{xx}}{\partial x}+\frac{1}{R}\times\frac{\partial N_{\theta x}}{\partial \theta}+q_x=I_1\frac{\partial^2 u_x}{\partial t^2} \tag{21}$$

$$\frac{\partial N_{\theta x}}{\partial x}+\frac{1}{R}\times\frac{\partial N_{\theta\theta}}{\partial \theta}+\frac{Q_{\theta r}}{R}+q_\theta=I_1\frac{\partial^2 u_\theta}{\partial t^2} \tag{22}$$

$$\frac{\partial Q_{xr}}{\partial x}+\frac{1}{R}\times\frac{\partial Q_{\theta r}}{\partial \theta}-\frac{N_{\theta\theta}}{R}+q_r=I_1\frac{\partial^2 u_r}{\partial t^2} \tag{23}$$

Where q_x، q_θ, , and $q_r$are the external load in peripheral, axial, and radial directions, and Q_{xr}، $Q_{\theta r}$, and I_1 are equal to

$$Q_{xr}=\frac{\partial M_{xx}}{\partial x}+\frac{1}{R}\times\frac{\partial M_{\theta x}}{\partial \theta} \tag{24}$$

$$Q_{\theta r}=\frac{\partial M_{\theta x}}{\partial x}+\frac{1}{R}\times\frac{\partial M_{\theta\theta}}{\partial \theta} \tag{25}$$

$$I_1=\int_{-\frac{h}{2}}^{+\frac{h}{2}}\rho_k\ dr \tag{26}$$

ρ_k is the volumetric mass related to each layer. Substituting the Equations (18) in (22), (23), and (24) results in the following equilibrium equations, where L_{ij} is the differential operator.

$$\begin{bmatrix}L_{11}&L_{12}&L_{13}\\L_{21}&L_{22}&L_{23}\\L_{31}&L_{32}&L_{33}\end{bmatrix}\begin{bmatrix}u\\v\\w\end{bmatrix}=\begin{bmatrix}-q_x\\-q_\theta\\-q_r\end{bmatrix} \tag{27}$$

Fully Simply Supported boundary conditions

The following defines the Fully Simply Supported boundary conditions for a cylindrical shell in $(x=0,l_x)$ and $(\theta=0,\gamma)$:

$$v=w=N_x=M_x=0 \qquad x=0,l_x \tag{28}$$

$$u=w=N_\theta=M_\theta=0 \qquad \theta=0,\gamma \tag{29}$$

To ensure that the assumed modes satisfy the boundary conditions u, v, and w, they are defined as the following double Fourier series [10]:

$$u=\sum_{m=1}^{\infty}\sum_{n=1}^{\infty}A_{mn}\cos\frac{m\pi x}{l_x}\sin\frac{n\pi\theta}{\gamma}T_{mn}(t) \tag{30}$$

$$v=\sum_{m=1}^{\infty}\sum_{n=1}^{\infty}B_{mn}\sin\frac{m\pi x}{l_x}\cos\frac{n\pi\theta}{\gamma}T_{mn}(t) \tag{31}$$

$$w=\sum_{m=1}^{\infty}\sum_{n=1}^{\infty}C_{mn}\sin\frac{m\pi x}{l_x}\sin\frac{n\pi\theta}{\gamma}T_{mn}(t) \tag{32}$$

Where A_{mn}, B_{mn}, and C_{mn} are the fixed coefficients of the mode shape, m is the is the number of longitudinal half-waves, n is the number of peripheral waves, and $T_{mn}(t)$ is the time-based function.

Results and Discussion

Natural frequency validation using references and ABAQUS software

The natural frequencies of the sandwich panel with fully simply boundary conditions for an integrated cylindrical shell of isotropic material were compared to the Lam and Loy research results. Lam and Loy presented their findings using the ω^* frequency parameter as follows:

$$\omega^*=R\omega\sqrt{\rho(1-\nu^2)E} \tag{33}$$

Where ω (rad/s) is the natural frequency, R is the cylindrical shell radius, ρ density, ν Poisson's ratio, and E is the Young's modulus.

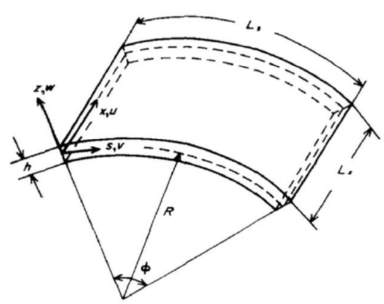

Fig. 4. Geometry and naming the characteristics of the cylindrical shell in the reference.

The frequency parameter values for a cylindrical shell with geometric characteristics $h/R=0/001$,

$\emptyset = 10^{\circ}$and $m = 1$ in Loy's research [10] are compared to the current research and finite element numerical analysis in Table 1. In all cases, finite element analysis was performed using the industry-standard ABAQUS software and the SC8R hexagonal element from the family of continuum shell elements. m and n are the number of axial- and peripheral- half sine waves, respectively.

Table 1. Comparing the frequency parameter present research and modeling (m = 1) ABAQUS.

	n=	n=	n=	n=	n=	n=
Lam and Loy [10]	0.05102	0	0.38776	1.9184	2.3878	3.5408
Present research	0.12342	0.04957	0.39948	1.90798	2.31865	3.60526
ABAQUS	0.12342	0.04751	0.39477	1.89946	2.30416	3.58239
Lam and Loy [10]	0.68367	0.77551	0.41837	1.1531	2.7245	0.9286
Present research	0.70308	0.90411	0.56502	1.11087	2.52843	3.81677
ABAQUS	0.70281	0.90316	0.56292	1.10632	2.52053	3.80351

The paper by Kalita and Halder was used to evaluate the results in the hollow state. The results for a flat sheet with a central hollow and fully simply supported boundary conditions, as illustrated in Fig. 5, were compared to the results from the current study on the shell. In fact, the flat sheet is a cylindrical shell with an infinite curvature radius of curvature $R \rightarrow \infty$ and an aperture angle $\emptyset \rightarrow 0$ close to zero.

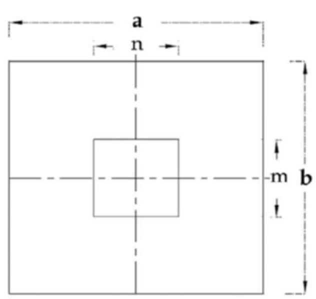

Fig. 5. Geometric sheet geometry studied in the study of Calita and Halder [11].

The frequency parameter and shape of the mode drawn in this study using the finite element solution in ABAQUS and the reference [11] are summarized in Table 2.

Table 2 The dimensionless frequency parameter $\omega^* = \omega a^2\sqrt{\rho h/D_{22}}$ for sheet with simply support and central cavity conditions $b/a = 1$، $h/a = 0.01$ ؛ $m = n = \frac{a}{5}$.

		Mode number	Mode number	Mode number	Mode number
		1	2	3	4
Solution Method	Total Mode	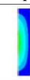	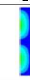		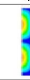
SWRI	Frequency Parameter	19.98	47.87	47.87	76.25
ABAQUS	Frequency Parameter	19.28	47.649	47.649	76.9
Present research	Frequency Parameter	20.4	49.3	49.3	77.6

The low percentage difference between the present results of the theory and those of ABAQUS and the reference [11] demonstrates that the present theory behaves correctly and logically in both the flat sheet and hollow states.

Parametric studies of free vibrations

The primary scheme is depicted in Figs. 1 and 2, along with the names of the various geometric variables for parametric analysis. As a result, all of the parameters examined are based on the name of this scheme, and the frequency parameter of representation of results, $\omega^* = \omega b^2\sqrt{\rho/(E_{22} \times h^2)}$. The frequency properties of sandwich cylindrical shells were investigated in this study. Table 3 shows a variety of integrated, reinforced, and unreinforced lattice shell geometries and materials with isotropic and orthotropic properties. It plotted the frequency parameter in terms of the wave numbers on both the outside and inside of the shells.

Table 3. Mechanical properties of isotropic and orthotropic materials used in parametric studies.

	E11GPA	E22GPA	V12	G12GPA	$\rho\ ^{kg}/_{m^3}$
isotropic	200	200	0.3	-	7800
orthotropic	60.7	24.8	0.23	12	1780

Figs. 6 and 7 illustrate the frequency analysis results for a cylindrical shell integrated with isotropic and orthotropic mechanical properties, respectively, where $^{h}/_{R} = 0/01$ γ، $= 90^{\circ}$ and $l_x = 1$. As shown in Fig. 8, the result of the same analysis for a unidirectional orthotropic cylindrical shell with no surface is 10*10 equal-sized hollows with a volume fraction of 10% (such as Figs 4 and 5). The cylindrical shell depicted in Fig. 10 also has a 10*10 lattice core and an orthotropic outer surface with the thickness of $h_{fu} = 0/1h$. Fig. 11 illustrates the effect of having two identical-thickness surfaces, $h_{fu} = h_{fd} = 0/1h$,at the top and bottom of the unidirectional lattice reinforcement.

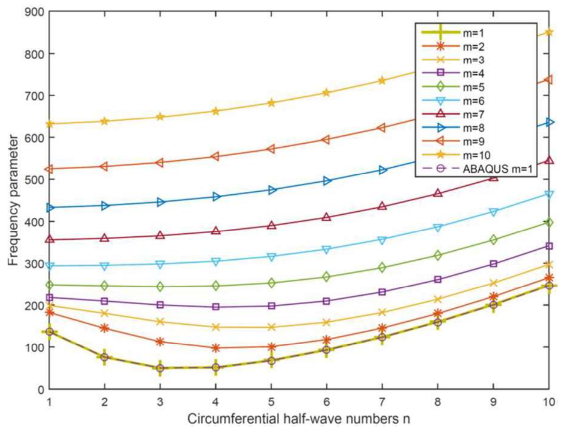

Fig. 6. Integrated isotropic cylindrical shell frequency parameter, according to the number of semicircular (n) and axial (m) semiconductor waves.

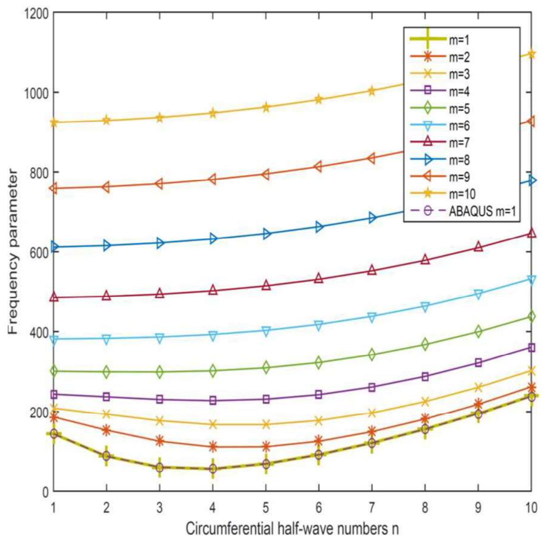

Fig. 7. The frequency parameter of the integrated orthotropic cylindrical shell, according to the number of semicircular (n) and axial (m) semicircular waves.

As illustrated in Figs. 6 and 7, the integrated shell with orthotropic properties, in addition to being significantly lighter than the same shell made of isotropic material, also has a higher natural frequency. Additionally, the fundamental frequency occurs when m=n=4 for the isotropic state and when m=1 and n=3 for the orthotropic state. Comparing the ABAQUS results for isotropic and orthotropic materials demonstrates the appropriate precision of the integrated geometry theory.

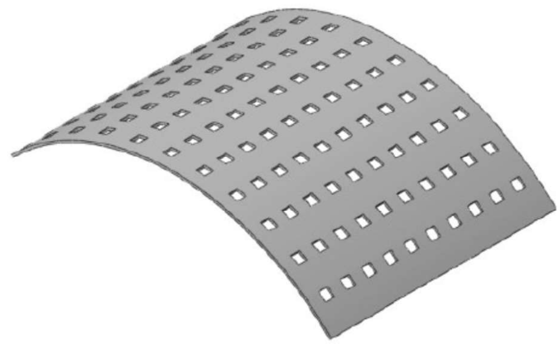

Fig. 8. Results of three- point bending test for composite plate

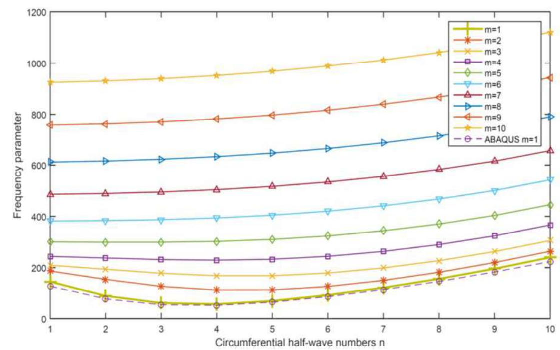

Fig. 9. Frequency Parametric Cylindrical Frequency Parameter (10*10) Single-directional orthotropic, in terms of the number of semicircular (n) and axial sinusoidal waves (m).

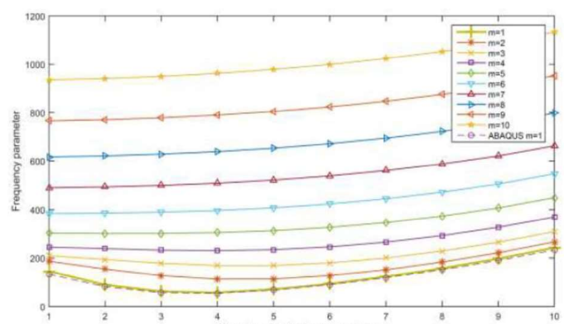

Fig. 10. One-way orthotropic frequency grid crust parameter frequency parameter (10*10) has an external procedure, in terms of the number of peripheral (n) and axial sinusoidal half-wave (m).

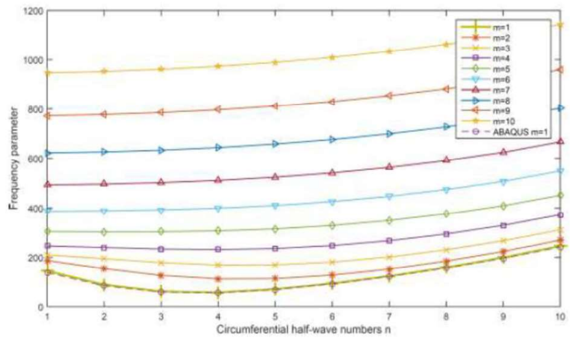

Fig. 11. Single-pole (10 10 10) single-direction orthotropic cylindrical shell frequency parameter has two approaches, in terms of the number of half-circumferential (n) and axial (m) axis sinusoidal waves.

As illustrated in Figs. 9, 10, and 11, when the shell geometry is changed from integrated to lattice, some differences occur as a result of the strong gradient of properties between the shell and the empty spaces, as well as the more pronounced effect of interlaminar shear. The difference between the results obtained with the present theory and those obtained with ABAQUS increases in the absence of the surfaces and decreases in their placement. Indeed, by positioning the surfaces both externally and internally to the lattice core, the interlaminar shear effect is reduced.

In orthotropic twisted string modeling (four zones), the fibers in the zero-degree ribs (longitudinal) have a zero-degree direction, while the fibers in the ninety-degree ribs (peripheral) have a ninety-degree direction (the orientation of the fibers is in the direction of longitudinal and peripheral ribs). However, in unidirectional orthotropic modeling (two-zone), the material of the lattice panel is only in one direction, and the rib concept does not apply. As illustrated in Fig. 12, a cylindrical lattice shell with 10*10 hollows configuration is considered for studying fiber modeling in the direction of the ribs. Figs. 13, 14, and 15 show the frequency parameter in terms of m and n for a lattice shell with no surface, a single surface, and a double surface, respectively. Each surface has a thickness of $h_f = 0.1h$.

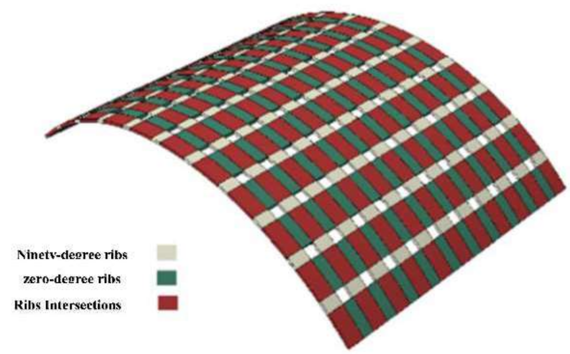

Fig. 12. Geometric shell geometry studied in screw orthotropic modeling.

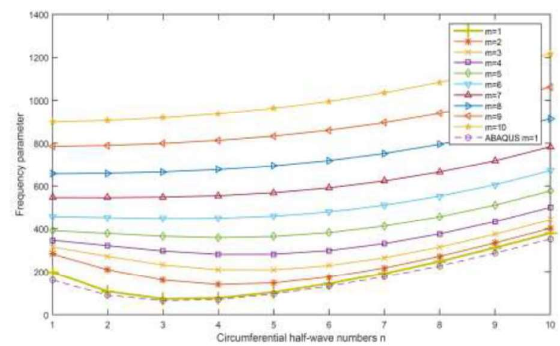

Fig. 13. The frequency parameter of the reticular cylindrical shell (10 10 10) of the aortic string orthotropic, in terms of the number of radial and axial radius (n) semiconductor waves.

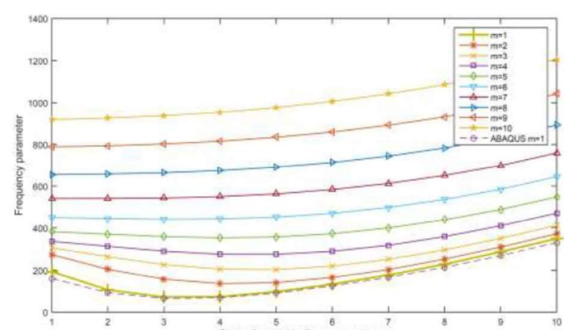

Fig. 14. The frequency parameter of the mesh cylindrical shell (10*10) of the orthotropic screw string has an external procedure, in terms of the number of half-wave radii (n) and axial (m).

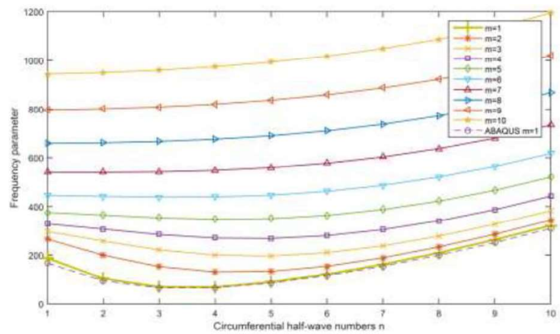

Fig. 15. The frequency parameter parameter of the mesh cylindrical shell (10 × 10) of the two-way screw orthotropic coil, in terms of the number of semicircular (n) and axial sinusoidal half-wave (m).

When the results of Figs. 13, 14, and 15 for twisted string modeling are compared to the results of Figs. 8, 10, and 11 for unidirectional modeling, it is clear that the difference between the results of the present theory and ABAQUS is greater for the twisted string mode than it is for the unidirectional model. This is because the gradient of material properties between the ribs and between the ribs and the knot increases, in addition to the gradient between the shell and the empty spaces, which increases shear between the layers. Additionally, the frequencies derived from twisted string modeling are greater than those derived from unidirectional modeling. This means that composite lattice shells formed using the twisted string method have a higher frequency than unidirectional lattice shells.

The effect of lattice shell aperture opening and panel length-to-chord ratio of $^{l_x}/_{b}$ on unidirectional orthotropic and twisted material has been investigated for lattice shell with parametric characteristics of $^{h}/_{R} = 0.01$, $\gamma = 90^{\circ}$, $l_x = 1$ and 10×10 number of hollows with 10% of volume fraction. The fundamental frequency results for the surface-less mode are shown in Figs. 18 and 19, while those for the single-surface lattice shell are shown in Figs. 16 and 17, and those for the lattice shell with bi-surfaces of each $h_f = 0.1h$ thickness are shown in Figs. 17 and 18. In each case, the modeling results were compared to those obtained using the ABAQUS finite element model.

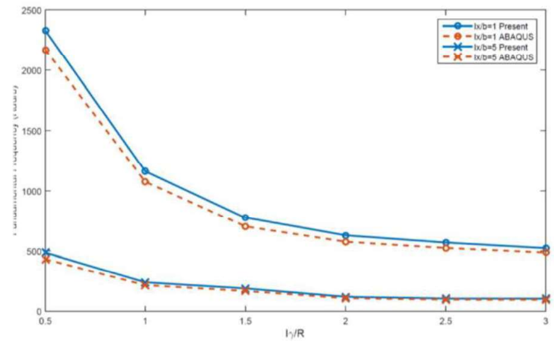

Fig. 16. The fundamental frequency of orthotropic lattice cylindrical shells (10*10 holes) single-way according to changes in the ratio of $^{l_\gamma}/_{R}$ and $^{l_x}/_{b}$

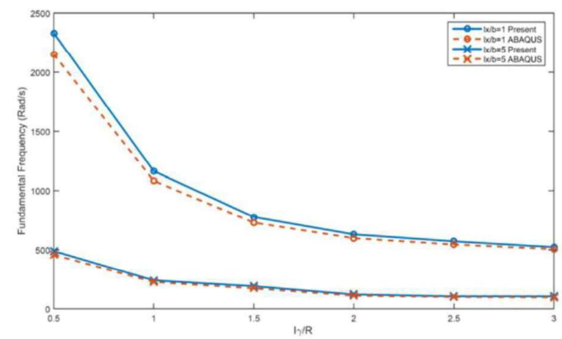

Fig. 17. The fundamental frequency of orthotropic lattice cylindrical shells (10 *10 holes) is one-way, with a procedure based on changes in the ratio of $^{l_x}/_{b}$ and $^{l_\gamma}/_{R}$

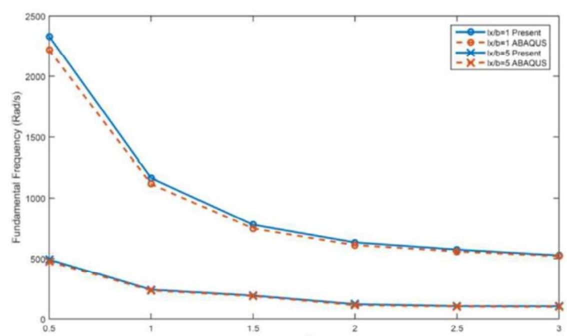

Fig. 18. The fundamental frequency of orthotropic lattice cylindrical shells (10 × 10 cavities) is one-way, with two procedures according to the changes in the ratio of $^{l_\gamma}/_{R}$ and $^{l_x}/_{b}$

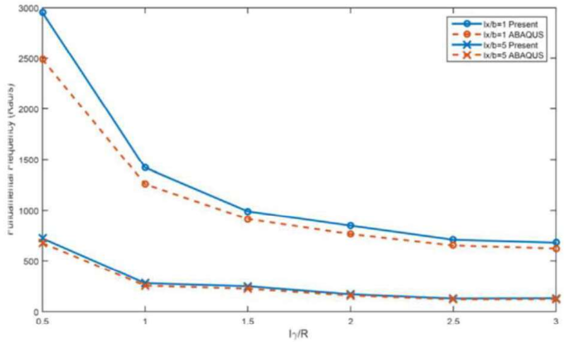

Fig. 19. The fundamental frequency of orthotropic lattice cylindrical shells (10 × 10 holes) of the coil, according to the changes in the ratio of $^{l_\gamma}/_R$ and $^{l_x}/_b$

According to Figs. 17, 18, and 19, the fundamental frequency variations for both cylindrical lattice panels with a length-to-chord ratio of ($^{\mathrm{l_x}}/_{\mathrm{b}} =$ 1 and $^{\mathrm{l_x}}/_{\mathrm{b}}$ begin with an insignificant aperture angle $\gamma = 1/5$ Rad value and converge to a specific value. Additionally, the natural frequency of the panel with $^{\mathrm{l_x}}/_{\mathrm{b}} = 1$ ratio is roughly four times that of the $^{\mathrm{l_x}}/_{\mathrm{b}} =$ 5 mode for the same amount of γ.

Shape drawing in three-dimensional mode

There are three natural frequencies (bending, torsional, and longitudinal) for each m and n, and each of these frequencies has a distinct mode shape. By examining the three-dimensional image of the shape of modes such as each and every one of them, it is possible to determine which of these natural frequencies this mode shape belongs to based on the relative deformation of the shell shape [10]. The orthotropic lattice panel $\gamma = 3$ rad $\mathrm{l_x} = 3\mathrm{m}$ 10×10 and $\mathrm{R} = 1\mathrm{m}$ in Fig. 20 has a hollows volume fraction ratio to the total volume of the panel of $\mathrm{V} = 20\%$ and a thickness of $\mathrm{h} = 0.01$ m. Fig. 21 depicts the mode shapes of this panel, including the fundamental frequency, as determined by ABAQUS, while Figs. 22 and 23 depict the mode shapes determined by the present theory.

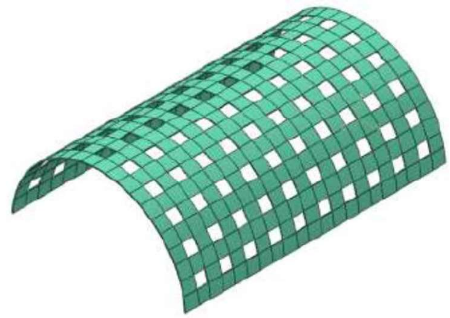

Fig. 20. Geometry of orthotropic lattice panel Number of cavities 10*10 and V = 20%.

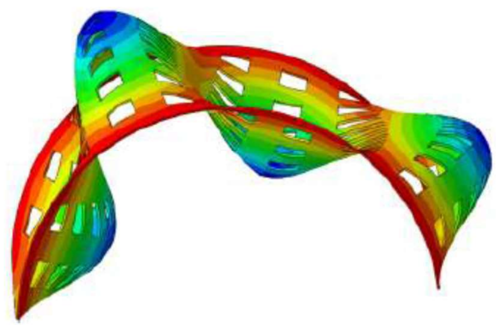

Fig. 21. The basic bending frequency mode shape of the retractable panel is obtained from ABAQUS.

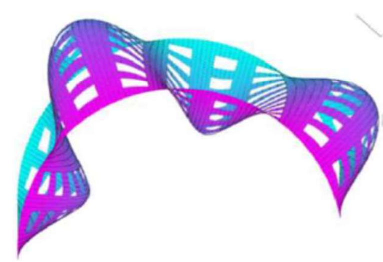

Fig. 22. The shape of the basic bending frequency mode of the lattice panel is obtained from the present study.

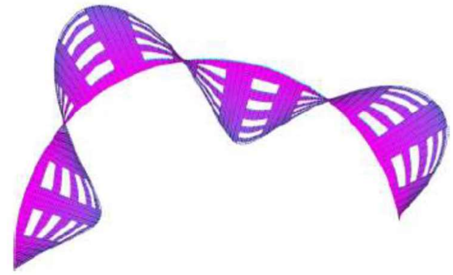

Fig. 23. The basic frequency frequency curve shape of the lattice panel is obtained from the present study (view from above).

Investigation of the results of forced shell vibrations with simply support conditions

The number of modes considered (m*n) in computer code is used to obtain the response (30*50). The values of m and n should be chosen in such a way that we arrive at the correct answer [13]. Coordinates of the load imposing location θ_l, x_l and the point on the shell where the response is calculated when the shell is in position ${}^{\gamma}/_{2}, {}^{l_x}/_{2}$.

Pulsation phenomenon

The pulsation phenomenon occurs as a result of the shell being subjected to an impulse load. Pulsation is a type of oscillation in which the amplitude of the oscillation increases and then decreases periodically [14]. We can observe this phenomenon by plotting diagrams of vibration amplitude variations in the radial direction to times many times larger than the normal period of the shell. The shell with fully simply supported boundary conditions $l_x = 1m$, $\gamma = °90$، $R = 1m$ and $h = 0.01m$, demonstrates this phenomenon in Fig. 24.

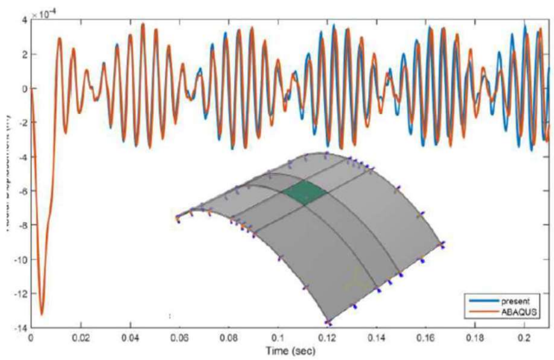

Fig. 24. Display the pulse phenomenon in the time response of the integrated panel with simple supportal and orthotropic properties, pulse type: sinusoidal $f_0 = -0.1\ MPa$ and load area $\theta_1 = 39°, \theta_2 = 51°)$ and $x_1 = 0.4m, x_2 = 0.6m)$.

Shell frequency response using Fourier transform

Vibrations detected from a structure are typically complex signals composed of several vibration signals of varying frequencies. Frequency analysis, alternatively referred to as Fast Fourier Transform (FFT) analysis, is a signal processing technique used to determine the frequency content of a vibrating signal. The horizontal axis of FFT-curves represents the frequency, while the vertical axis represents the amplitude of the vibration.

Occasionally, it is difficult to determine the number of natural frequencies present on a temporal response diagram of a vibrating system. The Fourier transform can be used to convert the time-domain response of a vibrating system to the frequency domain, yielding the system's frequency response spectrum and allowing for discussion of the system's natural frequencies [14]. Figs. 24 and 25 illustrate the studied frequency response of the shell. This method allows for the formation of frequencies excited by the impulse load applied to the shell. The dominant excitation frequency is equal to 180.7 Hz, as shown in this figure. The natural frequencies of this shell are illustrated in Fig. 26 in terms of the number of distinct longitudinal half-waves and the number of peripheral waves. As illustrated in this figure, the second frequency of the shell is 180.4 Hz and occurs at m=1 and n=3. Indeed, external excitation at a frequency close to one of the natural fundamental frequencies of the shell results in increased excitation of that frequency, such that the effect of other frequencies on the time-domain response can be considered negligible in comparison to that frequency's effect.

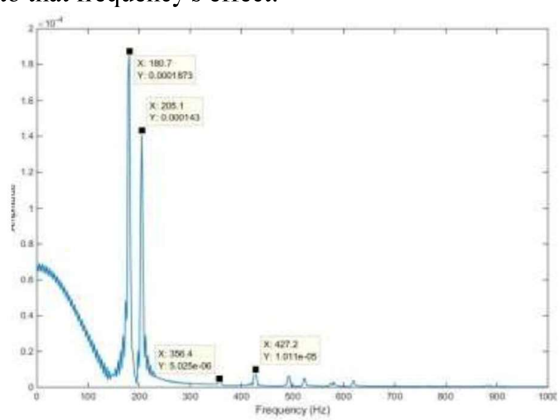

Fig. 25. Frequency response of the studied shell in Fig. 23.

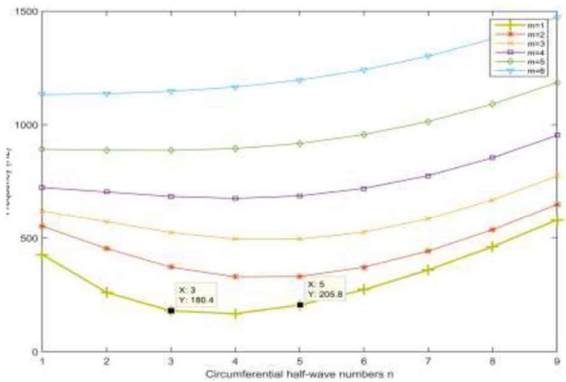

Fig. 26. The natural frequencies of the crust examined in Fig. 23.

Parametric studies of forced vibrations

As previously stated, geometric parameters such as the thickness-to-radius ratio $^{h}/_{R}$ and the aperture angle ratio of the panel to the radius $^{\gamma}/_{R}$ have an effect on the natural frequencies of the shell. As a result, they will affect the time-domain response of the shell. The effects of isotropic and orthotropic properties under step and triangular pulses on an integrated shell with geometric properties $l_x = 1m$, $\gamma = °90$.$R = 1m$ and $h = 0/01m$ are illustrated in Figs 27 and 28.

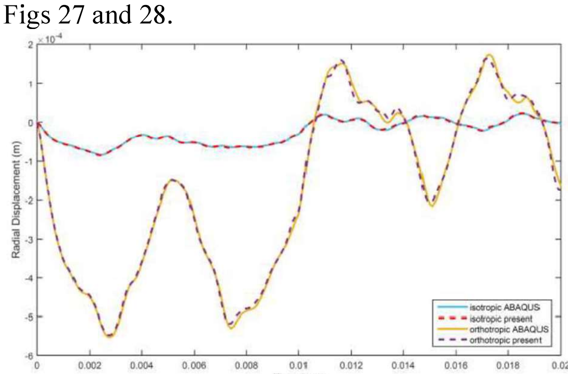

Fig. 27 Investigate the time response of the integrated panel with isotropic and orthotropic properties of pulse type: stairs $f_0 = -0.1\ MPa$ load area ($\theta_1 = 42°, \theta_2 = 48°$) and ($x_1 = 0.45m$, $x_2 = 0.55m$)

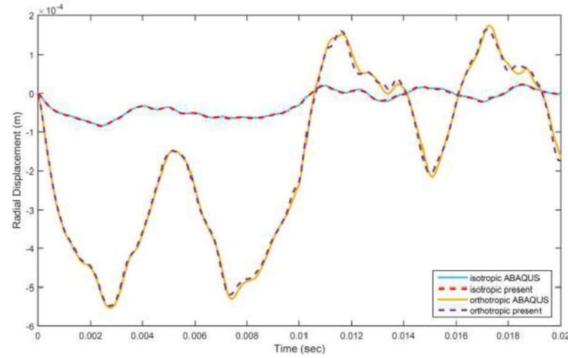

Fig. 28 Investigating the time response of the integrated panel with isotropic and orthotropic properties of pulse type: triangular ($f_0 = -0.1\ MPa$) load area ($\theta_1 = 42°, \theta_2 = 48°$) and ($x_1 = 0.45$, $x_2 = 0.55$)

The duration of the imposing load is t_1=0.01s in the modeling of Figs. 1 and 2, and as can be seen, the amplitude of the response of the shell with isotropic properties is significantly less than that of the shell with orthotropic properties for both loading pulses. Additionally, the overlap of the results from ABAQUS modeling and the present theory demonstrates the appropriate accuracy of the theory for the integrated shells.

The effect of the aperture angle-to-shell radius ratio on the variations in radial displacement over time for an orthotropic shell was investigated, and the results are shown in Fig. 29. The center of the panel in each of these shells is defined by the load center and the point at which displacement is plotted over time. Additionally, the area of the load imposing areas is one-sixteenth of the panel's area ($l_1 = l_2$). The amplitude of the vibrations at the aperture angle $\gamma = 1$ rad is the smallest and closest to zero after the load is imposed $t_1 = 0.01$ s.

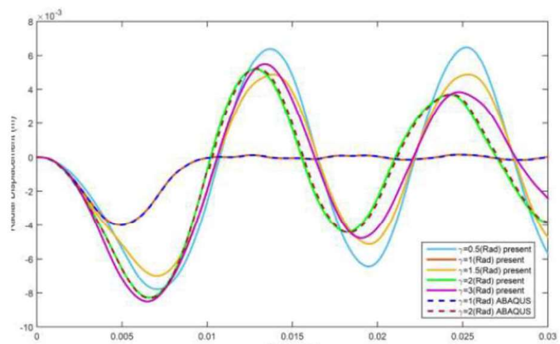

Fig. 29 Check the parameter γ on the time response of the panel with the orthotropic properties of the pulse type: sinusoidal $f_0 = -0.1\ MPa$ MPa, $l_x = ۲m$, R = 1m and h = 0.01m

Another study examined the effect of panel thickness when the aperture angle was $l_x = 2\mathrm{m}$ and $\gamma = 3\,\mathrm{rad}$. The location and area of the load imposing area are identical for all shells in this study, as shown in Fig. 30, and are located in the center of the panel. The output plotted represents the same point. Other geometry and load parameters remain unchanged.

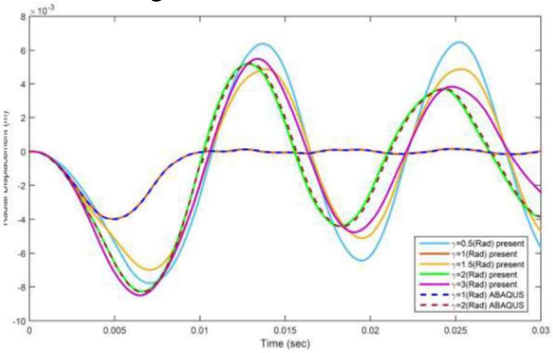

Fig. 30. Investigate the $^{h}/_{R}$parameter on the panel response time with orthotropic properties. Pulse type: sinusoidal $f_0 = -5000$ Pa.

Conclusion

The natural frequencies of an integrated and lattice composite cylindrical shell are affected by a variety of parameters, including the volume fraction of hollows, the configuration of the hollows, the thickness-to-radius ratio, and the length-to-radius ratio. The following text summarizes the effect of these parameters:

While the orthotropic panel is lighter in weight than the isotropic panel, it also has a higher fundamental frequency for the same geometry (as shown in Figs. 6 and 7.)

The percentage difference between the responses obtained from the present theory and ABAQUS is slightly increased for unidirectional and twisted orthotropic modeling. This percentage difference between twisted string modeling and modeling without a surface is greater than the percentage difference between unidirectional modeling and modeling with internal and bi-surfaces. By locating the surface on the outer or inner surface of the lattice panel, the effect of interlaminar shear is mitigated, and theoretical and numerical results become more comparable (as shown in Figs. 8 to 15.)

While orthotropic lattice panels made in the twisted method have the same mass matrix as unidirectional lattice panels, they have a higher rigidity, and thus have higher natural frequencies. The fundamental frequency of lattice cylindrical shells with smaller aperture angles is greater, and as the panel aperture angle increases, the fundamental frequency decreases until it is approximately constant near 1.5 radians. The fundamental frequency of the sandwich shell can be increased by locating one or two surfaces on the lattice panel (as shown in Figs. 18 and 19.)

For both unidirectional and twisted lattice modeling, the trend toward increasing the fundamental frequency is greater than the trend toward increasing the thickness of shells with a smaller aperture angle, and the thicker the panel.

The transient dynamic response of a composite cylindrical shell with fully simple boundary conditions is dependent on a number of parameters, including the thickness-to-radius ratio, the length-to-radius ratio, the material's isotropic and orthotropic properties, and the loading mode. These parameters have the following effect:

When the excitation frequency is close to the natural frequencies of the shell, the pulsation phenomenon manifests itself in the time-domain response of the shell. It is possible to investigate the dominant frequencies in the shell response by examining temporal responses in the frequency domain.

When two shells of identical geometry are loaded, the shell with isotropic properties exhibits a lower amplitude response than the shell with orthotropic properties.

The amplitude of the shell vibration decreases as the thickness-to-radius ratio increases, and the maximum amplitude of the shell vibration occurs earlier.

By and large, increasing the fundamental frequency value decreases the maximum value of the shell vibration amplitude and accelerates the time-domain response of the shell. As the fundamental frequency decreases, the maximum value of the vibration amplitude of the shell increases, the time-domain response of the shell becomes slower, until it reaches the fundamental frequency. The increase or decrease in fundamental frequency can be attributed to a variety of factors, including variations of the length-to-radius ratio, thickness-to-radius ratio, and etc.

References

[1] K. Suzuki, "Vibrations of Composite Circular Cylindrical Vessels," vol. 35, no. 22, pp. 2877–2899, 1998.

[2] C. T. Loy. D. K. Y. Lam, "Influence of boundary conditions for a thin laminated rotating cylindrical shell," Compos. Struct., vol. 41, no. 1, pp. 215–228, 1998.

[3] X. M. Zhang, G. R. Liu, and K. Y. Lam, “Vibration analysis of cross-ply laminated composite cylindrical shells using the wave propagation approach,” Appl. Acoust., vol. 62, no. 3, pp. 229–243, 2001.
[4] Y. Lee, M. Choi, and J. Kim, “Free vibrations of laminated composite cylindrical shells with an interior rectangular plate,” vol. 265, pp. 795–817, 2003.
[5] Ö. Civalek, “Numerical analysis of free vibrations of laminated composite conical and cylindrical shells: Discrete singular convolution (DSC) approach,” vol. 205, pp. 251–271, 2007.
[6] M. S. Qatu and E. Asadi, “Vibration of doubly curved shallow shells with arbitrary boundaries,” Appl. Acoust., vol. 73, no. 1, pp. 21–27, 2012.
[7] E. Ghavanloo , S. A. Fazelzadeh, “Free vibration analysis of orthotropic doubly-curved shallow shells based on the gradient elasticity,” Compos. Part B Eng., vol. 45, no. 1, pp. 1448–1457, 2013.
[8] Li, Guoqiang, and Jinquan Cheng. "A generalized analytical modeling of grid stiffened composite structures." Journal of Composite Materials 41.24 (2007): 2939-2969.
[9] Qatu, Mohamad Subhi. Vibration of laminated shells and plates. Elsevier
[10] Lam, K. Y., and C. T. Loy. "Vibration characteristics of thin cylindrical panels." Applied Acoustics 42.4 (1994): 347-359.
[11] E. Ghavanloo and S. A. Fazelzadeh, “Free vibration analysis of orthotropic doubly-curved shallow shells based on the gradient elasticity,” Compos. Part B Eng., vol. 45, no. 1, pp. 1448–1457, 2013.
[12] Stefan Markus, “The mechanical of vibration cylandrical shells”, Elsevier, Amesterdam-Oxford-New York-Tokyo-1988. of rectangular plates with central cutout." Cogent Engineering 3.1 (2016): 1163781.
[13] Y.-S. Lee and K.-D. Lee, “On the dynamic response of laminated circular cylindrical shells under impulse loads,” Comput. Struct., vol. 63, no. 1, pp. 149–157, 1997.
[14] Singeresu S Rao., “Mechanical Vibration” 1985.